



Mechanism of continuous dynamic recrystallization of Ti–6Al–4V alloy during superplastic forming with sub-grain rotation

Jun-zhou YANG, Jian-jun WU, Hai-nan XIE, Zhi-guo LI, Kai-wei WANG

School of Mechanical Engineering, Northwestern Polytechnical University, Xi'an 710072, China

Received 6 November 2021; accepted 31 March 2022

Abstract: The continuous dynamic recrystallization (CDRX) mechanism of Ti–6Al–4V alloys during the superplastic forming (SPF) was investigated, aiming to clarify the dominant mechanism for various misorientation evolution processes. The tensile tests were designed at 890, 920, and 950 °C with 10^{-4} – 10^{-2} s⁻¹, the electron back-scattered diffraction (EBSD) observations and constitutive model were applied to describing the microstructure evolution. The geometrically necessary dislocations (GNDs) are responsible for the low angle grain boundaries (LAGBs) evolution. Furthermore, the mechanism of the transformation from LAGBs to high angle grain boundaries (HAGBs) includes: (1) the migration from HAGBs to LAGBs; (2) the remaining dislocations after dynamic recovery will move to the LAGBs; (3) the sub-grain rotation also promotes the grain nucleation. Based on the physical constitutive model, the sub-grain rotation is verified just before the transformation from LAGBs to HAGBs. Particularly, the dislocation motion is dominant before the misorientation reaches the saturated value during the grain boundary misorientation evolution, otherwise, the sub-grain rotation will be activated.

Key words: continuous dynamic recrystallization; sub-grain rotation; grain boundary misorientation; superplastic deformation

1 Introduction

For fighter and civil aircraft, nearly 10%–34% of the body structural materials are titanium alloys [1–3]. The Ti–6Al–4V alloy is extensively applied, due to its low density, high specific strength, excellent corrosion resistance, etc [4–6]. Superplastic forming (SPF) has always been employed in the manufacturing of parts with complex shapes and geometries [7–10]. For Ti–6Al–4V alloy, the forming temperatures are about 900 °C, the strain rates need to be controlled in the range of 10^{-4} – 10^{-2} s⁻¹ [11]. Recently, the interest of superplasticity has focused on the accommodated mechanisms of grain boundary sliding (GBS): dislocation mechanism [12–15], diffusional mechanism [16–18], etc [19,20]. The

deformation mechanisms are the basis for the study of flow behavior and forming process optimization.

There are two compulsory requirements in the SPF process: high temperature and low strain rate [21], and both would accompany by high cost. Controlling chemical compositions of the alloy has successfully optimized the superplasticity [22], but similar research is rare, and this method is difficult to categorize and analyze systematically. The more mainstream method is still to reduce the deformation temperature by refining the grains [23,24]; however, some reasons would limit the development of this application: (1) additional expenses for the complex process of refining grains cannot be ignored; (2) the barriers of grain size lower than limits are hard to overcome; (3) static and dynamic grain growth mechanisms make it complex to design the grain sizes [25,26]. Therefore, a feasible path is to

explore a balance between grain refinement and optimization of superplasticity, which requires more attention to grain growth mechanisms. This work focused on the dynamic recrystallization behaviors during superplastic deformation.

ALABORT et al [27] gave a deformation map of Ti–6Al–4V alloy based on the strain rate sensitivity factors. For the specimens tested in the DRV region at 900 °C with a strain rate of $1 \times 10^{-4} \text{ s}^{-1}$, the grain size still decreases and the DRV process can still occur simultaneously. So, the continuous dynamic recrystallization (CDRX) should be responsible [28,29]. However, the dominant mechanism at other deformation temperatures and strain rates is discontinuous dynamic recrystallization (DDRX). Overall, whether the DRX process is CDRX or DDRX is still controversial. In addition, the initial grain sizes during the superplastic deformation can affect both processes. MATSUMOTO et al [30–32] proposed a mechanism that the DRV of titanium alloys should be influenced by grain sizes [30], phase compositions [31], and grain growth process [32]. Therefore, the mechanism of grain refinement may be tangled for various grain sizes. One of the objectives of this study is to clarify the DRX mechanisms during superplastic deformation. The other issue is the constitutive model of the DRX process, and a brief review will be given in this section. The DDRX model is very mature, can describe the grain size evolution [27,33], and the deformation mechanism deduced from the model calculation results is also relatively reliable [21,34]. However, the CDRX models are much more complex, and several typical models have been established [35–37]. The consensus is that the increment of the grain boundary angle misorientation is accompanied by sub-grain rotation; however, the dominant misorientation evolution mechanism is not clear. Another aim of this work is to explore the explicit mechanism of sub-grain rotation misorientation.

Based on the gaps in the DRX process, the objective of this study is to investigate the grain refinement mechanism of Ti–6Al–4V alloy. It is mainly divided into three parts: (1) a series of tensile tests and microstructure observations are performed to explore the evolutions of grain boundary misorientation distribution; (2) the effects of sub-grains rotation on grain boundary

misorientation are discussed; (3) a recrystallization mechanism is given based on the calculated results of constitutive model.

2 Experimental

The 1 mm thick Ti–6Al–4V alloy sheet in this work was investigated. Based on the results of energy dispersive spectrometry (EDS), the chemical compositions are listed in Table 1. As shown in Fig. 1 by scanning electron microscopy (SEM), the as-received alloys consist of abundant equiaxed α -phase grains, and the β -phase grains are interspersed among the equiaxed grains. This is a typical microstructure for superplastic deformation, where equiaxed grains are beneficial to the GBS.

Table 1 Chemical compositions of as-received material (wt.%)

Ti	Al	V	C
88.31	5.59	4.85	1.25

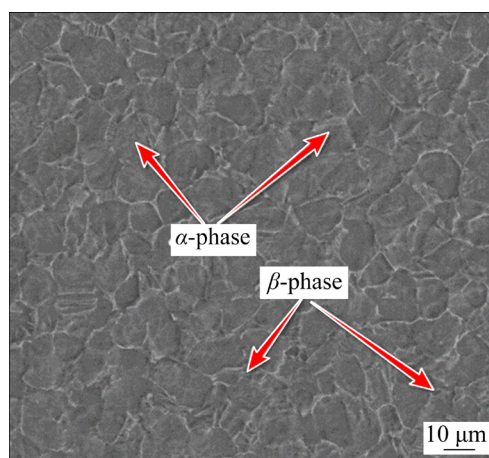


Fig. 1 Initial microstructure of as-received material

The high-temperature tensile test specimens were cut by the wire cut electrical discharge machining (WEDM), and the dimensions are given in Fig. 2. The constant strain rate tensile tests were performed on the Shimadzu electronic universal testing machine according to the GB/T 4338—2006. This tensile machine with three controlled heating zones in the heating furnace ensured that the temperatures of the specimens were maintained uniformly during the deformation process. The selected temperatures during the experiments were 890–950 °C with 30 °C intervals, and strain rates were ensured at 1×10^{-2} , 1×10^{-3} , and $1 \times 10^{-4} \text{ s}^{-1}$. The

samples were heated to the set temperatures with a heating rate of 5 °C/s. Five min delay was set from reaching the set temperature to the test beginning, which was designed to obtain the uniform temperatures and textures. To ensure good contact between the specimens and the thermocouples, each specimen must be manually ground with 1000# sandpaper before the tensile tests. Besides, the experiments for the strains of 0.2, 0.5, and 0.8 at each temperature were also implemented to observe the evolution on the intermediate states.

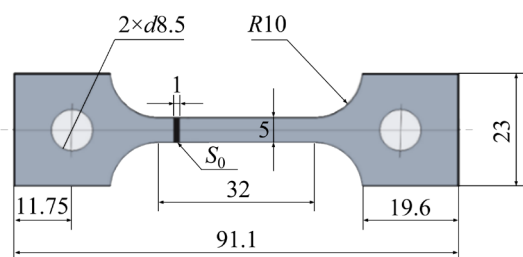


Fig. 2 Dimensions of tensile test specimens (S_0 is the cross-section) (unit: mm)

The microstructure evolutions were studied by a series of electron back-scattered diffraction (EBSD) observations. Measurements were carried out on an SU3500 scanning electron microscope equipped with an Oxford energy spectrum and EBSD camera. The EBSD results were analyzed by the Channel 5 software, and the differentiated orientation difference between HAGBs and LAGBs was 15°. All metallographic samples were cut from tensile specimens before and after testing. EBSD observations were used to identify the grain sizes and the evolution of grain boundary misorientations. The samples were prepared by electrolytic polishing, and the electrolyte composition was $V(\text{HClO}_4):V(\text{CH}_3\text{OH}):V(\text{CH}_3(\text{CH}_2)_3\text{O})=3:32:15$. The polished voltage was 22 V on the Struers Lectropol-5 for 40 s.

3 Results and discussion

3.1 Initial microstructure

Figure 3 shows the initial microstructures by EBSD Z -axis micrograph. In Fig. 3(a), the initial mean grain size of equiaxed grains is 3.77 μm . The red, green, and blue colors represent the $\langle 0001 \rangle$, $\langle \bar{1}2\bar{1}0 \rangle$, and $\langle 10\bar{1}0 \rangle$ crystallographic directions, respectively. There are more red grains for the initial inverse pole figure (IPF), indicating that most grains are in the $\langle 0001 \rangle$ direction. Therefore, the

initial material should have a preferred orientation. This can be more intuitively observed in Fig. 3(b). In the pole figures (PF), the maximum multiple of the uniform density (MUD) of received material is 6.60, and the characteristics of the basal texture can be observed. Besides, Fig. 3(c) shows the distributions of the HAGBs in black lines and LAGBs in red lines, and the relative frequency and cumulative frequency of the grain boundary misorientation angle are given in Fig. 3(d). There are 26% LAGBs due to the insufficient annealing of the material during the sheet manufacturing process. In Fig. 3(e), the compositions of the initial grains are divided into three categories: deformed grains in red color, substructures in yellow color, and recrystallized grains in blue color. The recrystallized grains are in majority, so the dynamic recrystallization (DRX) will occur during the rolling deformation, and substructures are connected in pieces. Besides, the kernel average misorientation (KAM) map demonstrates that misorientations exist in the substructures [38], and these misorientations can be observed both within the grains and near the grain boundaries. Larger KAM values represent higher geometrically necessary dislocations (GNDs) densities [38,39]. As indicated by the yellow arrow in Fig. 3(f), the large KAM values are more concentrated at the HAGBs except the deformed grains, indicating that dislocations densities near these areas are higher than those in inner grains.

3.2 Evolution of grain boundary misorientation distribution

The microstructure constitutions for Ti–6Al–4V alloy after tensile testing at 920 °C and $1 \times 10^{-3} \text{ s}^{-1}$ are shown in Fig. 4. The dislocation annihilation is effective when the DRV mechanism is dominant, and DDRX may be difficult to occur due to the unattainable critical dislocation density. Grain nucleation can nearly be observed, so the CDRX needs to be noticed undoubtedly [40,41]. CDRX usually occurs when the material has high stacking faculty energy or the deformation with large strain. For the strain of 0.5, it can be observed that the substructures are relatively dispersed. As is shown in Fig. 5, the area fraction of the LAGBs accounts for 49%, which is larger than that of the initial material. In addition, substructures distribution becomes fragmented from each other.

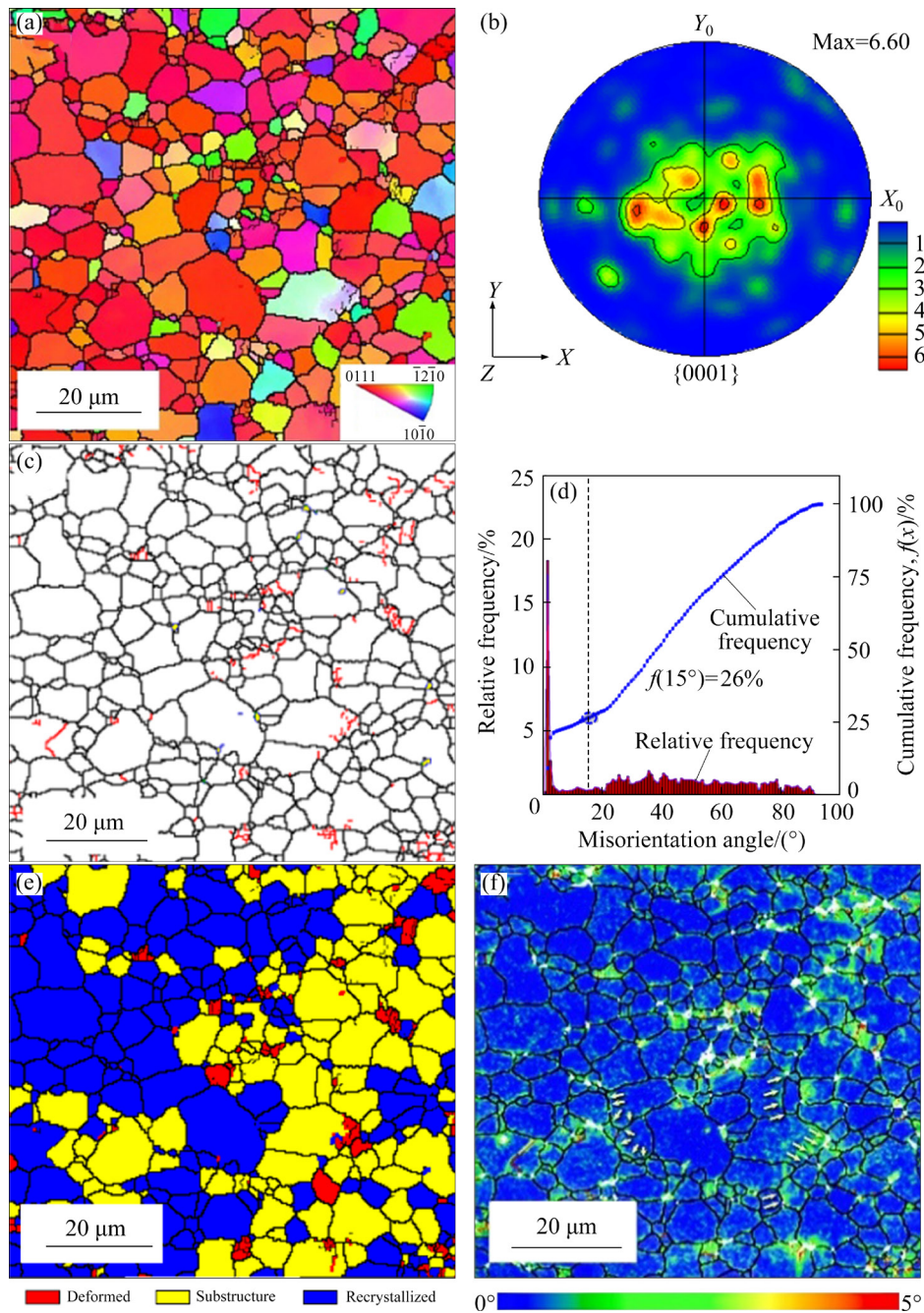


Fig. 3 Initial microstructures of material before tensile tests: (a) IPF map; (b) PF map; (c) Grain boundaries map; (d) Relative frequency and cumulative frequency of misorientation angles; (e) Microstructure constitution map; (f) KAM map

Ignoring the uneven distribution of grain boundaries, the LAGBs within the grains are rearranged during the initial stage. When $\varepsilon=0.8$, some recrystallized grains have transformed into substructures in Fig. 4(b). Besides, deformed grains can always be found around the substructures, indicating that the LAGBs are also related to plastic deformation. A similar conclusion has been obtained by PATNAMSETTY et al [42] that DRX grains undergo simultaneous deformation, and then

substructures occur. Correspondingly, the area fraction of LAGBs accounts for 76% in Fig. 5(b), reaching a very high level. Subsequently, with the continued deformation, the substructure grains transform into recrystallized grains again. The recrystallized grains are formed when LAGBs translate to be larger than 15° , which is the interfaces with local misorientation angles (θ) of HAGBs (exceeding 15°) and LAGBs ($2^\circ-15^\circ$) [43]. This process is because the misorientations of the

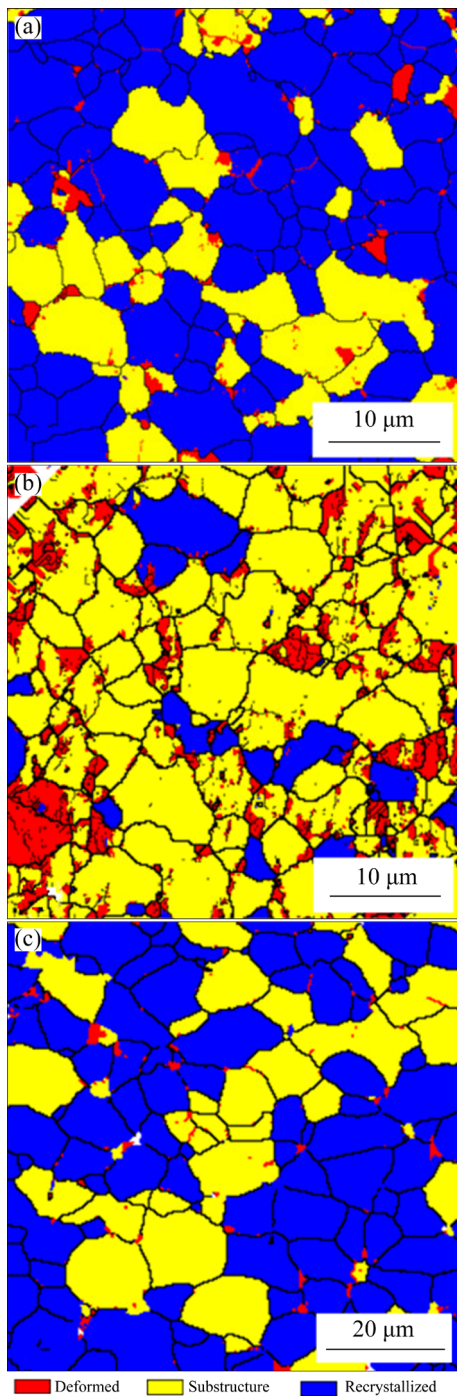


Fig. 4 Microstructure constitutions after tensile testing at 920 °C and $1 \times 10^{-3} \text{ s}^{-1}$: (a) $\epsilon=0.5$; (b) $\epsilon=0.8$; (c) $\epsilon=2.71$

sub-grain boundaries gradually increase, and the proportion of LAGBs is reduced to 35%. To sum up, grain refinement is a process of grain boundary redistribution.

3.3 Geometrically necessary dislocations and LAGBs

In Fig. 6(a), different grain boundary angles have been distinguished with several colors. This

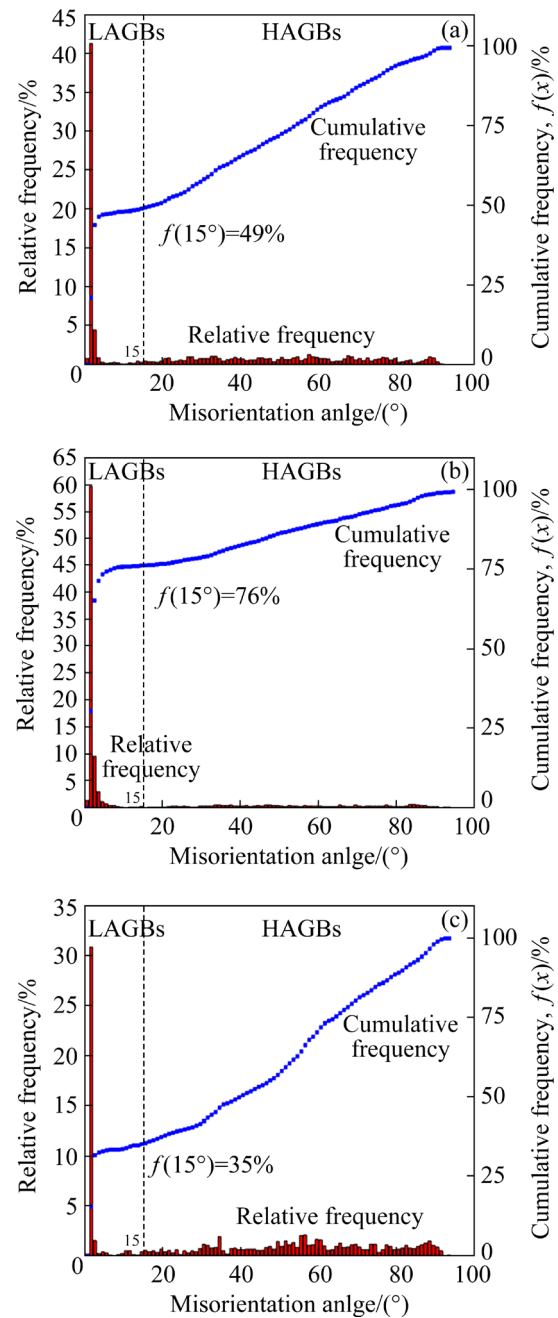


Fig. 5 Grain boundary misorientation angle distributions after tensile testing at 920 °C and $1 \times 10^{-3} \text{ s}^{-1}$: (a) $\epsilon=0.5$; (b) $\epsilon=0.8$; (c) $\epsilon=2.71$

result shows discontinuous grain boundary angles in different regions, which may be caused by insufficient resolution in the EBSD tests. The gray area is the α -phase, and the yellow area is the β -phase, which distributes at the junctions among the HAGBs, or the sub-grains are surrounded by LAGBs and HAGBs. The GNDs density was also calculated with the technology of the MTEX toolbox. MTEX is a free Matlab toolbox for analyzing the EBSD results or pole figure data, and

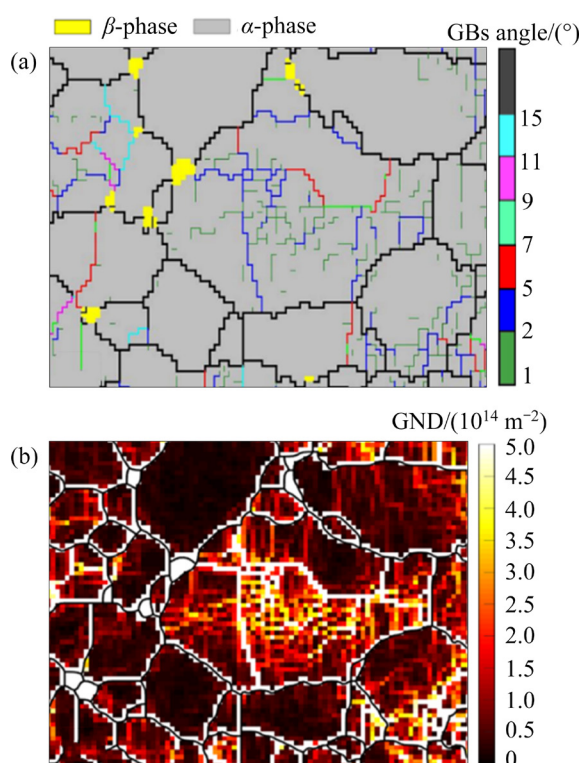


Fig. 6 Distribution of microstructures in Ti-6Al-4V alloy after tensile test at 920 °C and $1 \times 10^{-2} \text{ s}^{-1}$: (a) Grain boundary misorientation; (b) GNDs distribution

the method to estimate the dislocation densities via dislocation density tensors is referred to in the discussion by PANTLEON [44]. The details of the GNDs map for Ti-6Al-4V alloy at 920 °C and $1 \times 10^{-2} \text{ s}^{-1}$ are given in Fig. 6(b). The evolutions of the local misorientation are transformed by absorbing the nearby dislocations [45]. This shows that the distributions of LAGBs and the high GNDs area overlap very well, so it can be inferred that the evolution of dislocation density during recrystallization is consistent with the evolution trend of GNDs. In other words, the LAGBs may be formed by GNDs. The LAGBs can prevent the dislocation motions and accumulate the dislocation densities, and the misorientation of the LAGBs increases and then converts into HAGBs. In summary, the GNDs during the deformation are the sources of LAGBs. Then, with the accumulation of dislocations at sub-grain boundaries, the LAGBs transfer into HAGBs, thus fine grains occur.

3.4 Evolution of KAM map

Figure 7 shows the KAM figure of Ti-6Al-4V alloy after tensile tests at 920 °C and $1 \times 10^{-2} \text{ s}^{-1}$,

where the black lines are HAGBs, and the red lines are LAGBs. After deformation, the dislocations in the grains are mainly concentrated near the LAGBs, which are inconsistent with initial dislocations near the HAGBs. That is to say, the dislocations that lead to the increase in the misorientation of the LAGBs are partly from the migration of the HAGBs.

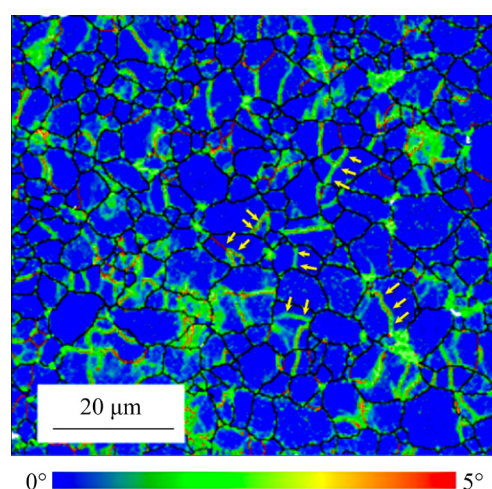


Fig. 7 KAM figure of Ti-6Al-4V alloy after tensile test at 920 °C and $1 \times 10^{-2} \text{ s}^{-1}$

4 Sub-grain rotation during CDRX

4.1 Grain orientation and misorientation of grain boundary

To further discuss the CDRX process, two crystal grains (Grains A and B) are extracted separately, as shown in Fig. 8. The CDRX process of Grain A is about to be completed, and three new recrystallized grains have been formed: A1, A2, and A6, with three sub-grains A3, A4, and A5, respectively. Grain B is still in the LAGBs evolution process, and there are five sub-grains: B1–B5. The orientation diagrams of Grains A and B are obtained by MTEX tool, the hexagonal prisms are used to indicate the hexagonal close-packed (HCP) crystal system, the yellow indicates the (0001) crystal plane and the blue indicates the (10 $\bar{1}$ 0) plane. For Grain B, there is no obvious change in the orientation between sub-grains, which are expressed by the same hexagonal prism. In the PF of Grain B, the orientation projections of Sub-grains B1–B4 are coincident. Therefore, the LAGBs in grains do not have significant effects on the orientation of the crystal grains. On the contrary, there is a little difference in orientation between the recrystallized crystal grains from Grain A, and they

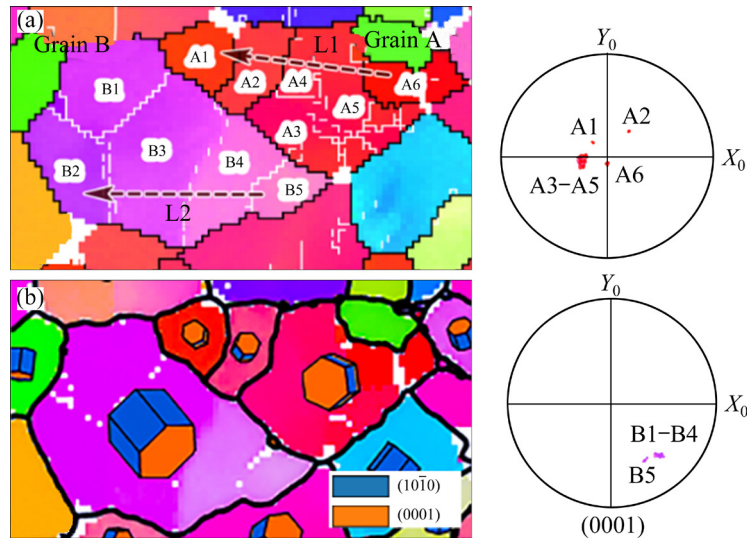


Fig. 8 Microstructure of Grains A and B after tensile test at 920 °C and $1 \times 10^{-2} \text{ s}^{-1}$: (a) Distributions of LAGBs and HAGBs; (b) Orientation diagrams in MTEX

are described by three prisms. In the PF map of Grain B, different sub-grain orientation projections are more clearly described. Since A3–A5 are divided by LAGBs, there is no obvious difference in orientation between these three small grains. Therefore, the following conclusions can be drawn: during the evolution from LAGBs to HAGBs, the rotation between recrystallized grains will occur.

Then, the misorientation angles of LAGBs and HAGBs are also given in Fig. 9. In Grain A, the dotted arrow L1 is A6 pointing to A1. The passing grain boundaries are: $19.64^\circ / \langle 2\bar{1}\bar{1}1 \rangle$, $54.80^\circ / \langle \bar{5}14\bar{3} \rangle$, and $30.15^\circ / \langle 0\bar{2}21 \rangle$. The misorientation angle of the first HAGB at $2.23 \mu\text{m}$ is 19.64° , which is very close to the critical angle of 15° . It can be considered that this grain has just been formed, but its orientation is already different from the parent grain. To some extent, it shows that there are sub-grain rotations during the CDRX. Since the grain refinement within Grain B is not completed, only LAGBs are observed to pass through the L2 (B5 to B2) path: $9.01^\circ / \langle \bar{1}\bar{1}2\bar{1} \rangle$, $3.13^\circ / \langle \bar{1}\bar{1}29 \rangle$, and $3.38^\circ / \langle 4\bar{1}50 \rangle$. Besides, the misorientation angles of the LAGBs are larger than those of the nearby areas, showing local peaks. This indicates that nearby dislocations, residual dislocations of insufficient DRV will move to the positions of LAGBs during the formation.

4.2 Constitutive model for CDRX

During the superplastic deformation of Ti–6Al–4V alloy, the grain growth will be affected by

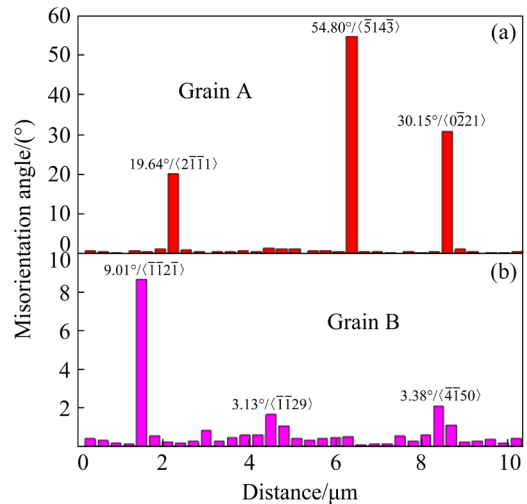


Fig. 9 Misorientation angles along L1 in Grain A (a) and L2 in Grain B (b) in Fig. 8(a)

the static grain growth, dynamic grain growth, and CDRX. As is listed in Eq. (1), a constitutive model is employed to describe the evolution of grain size and grain boundary misorientations, which is based on the literature [36,46–48].

$$\begin{cases} \dot{d} = \beta_1 d^{-\gamma_1} + \beta_2 \dot{\epsilon}_p d^{-\gamma_2} - \beta_3 \dot{\rho}^{\gamma_4} d^{-\gamma_3} \\ \dot{\bar{\rho}} = \beta_4 (S_{H_0} / S_H)^{\gamma_5} (1 - \bar{\rho}) \dot{\epsilon}_p - \alpha_1 \bar{\rho}^{\gamma_6} - \alpha_2 S \bar{\rho}^{\gamma_7} \\ \dot{S}_L = \alpha_4 \bar{\rho}^{\gamma_8} \dot{\epsilon}_p - \beta_5 S_L \dot{\bar{\theta}}_{sub} - \\ \alpha_3 S_L^2 \bar{\theta}_{sub}^{\gamma_9} (1 - \ln \bar{\theta}_{sub}) \bar{\rho}^{\gamma_9} - \alpha_5 S_L \bar{\rho}^{\gamma_{10}} S_H \\ \dot{S}_H = \beta_5 S_L \dot{\bar{\theta}}_{sub} + \alpha_3 S_L^2 \bar{\theta}_{sub}^{\gamma_9} (1 - \ln \bar{\theta}_{sub}) \bar{\rho}^{\gamma_9} - \\ \alpha_2 S_H^2 \bar{\rho}^{\gamma_{10}} \\ \dot{\bar{\theta}}_{sub} = \alpha_6 \dot{\epsilon}_p \bar{\rho}^{\gamma_{11}} S_L^2 \bar{\theta}_{sub} (\theta_r \bar{\theta}_{sub} - 1) \ln(n \bar{\theta}_{sub}) \end{cases} \quad (1)$$

where d is the grain size, S_H and S_L represent the areas of HAGBs and LAGBs, respectively. γ_i and γ_θ are the material constants. S_{H_0} is the initial S_H for annealed material. $\bar{\rho}$ is normalized dislocation density, and defined by $\bar{\rho}=(\rho-\rho_i)/\rho_s$, ρ_i is the initial dislocation density, and ρ_s is the saturated dislocation. $\bar{\theta}_{sub}$ is the normalized misorientation angle, $\bar{\theta}_{sub}=\theta_{sub}/\theta_c$, and θ_c is the critical misorientation angle. $\theta_r=\theta_c/\theta_{sat}$, θ_{sat} is the steady value of the average misorientation angle for sub-grains, and $\theta_{sat}=4^\circ-8^\circ$; $n=\theta_c/\theta_m$, θ_m is the misorientation angle for grain boundaries with maximum energy, and $\theta_m=20^\circ-25^\circ$. The temperature-dependent parameters are denoted as follows:

$$\left\{ \begin{array}{l} \alpha_1 = C_{a_1} \exp\left(-\frac{Q_a}{RT}\right) \\ \alpha_2 = \frac{C_{a_2}}{T} \exp\left(-K_g T - \frac{Q_b}{RT}\right) \\ \alpha_3 = \frac{C_{a_3}}{T} \exp\left(-K_g T - \frac{Q_b}{RT}\right) \\ \alpha_4 = C_{a_4} \exp\left(-\frac{Q_a}{RT}\right) \\ \alpha_5 = C_{a_5} \exp\left(-\frac{Q_a}{RT}\right) \\ \alpha_6 = C_{a_6} \exp\left(-\frac{Q_a}{RT}\right) \end{array} \right. \quad (2)$$

where Q_a is the thermal activation energy, and Q_b is the activation energy of grain boundary self-diffusion. Some material constants have been

reported: $K_g=5.4\times 10^{-4} \text{ K}^{-1}$, $\theta_c=15^\circ$ [46,49]. The other material parameters are needed to be determined by the multi-objective genetic algorithm (GA) [50], and the results are listed in Table 2.

4.3 Calculation by constitutive model

The comparison between the experimental data and predicted results of grain sizes is presented in Fig. 10. Dots represent the experimental grain sizes, and the solid line represents the prediction results. Besides, the grain size–strain curves obtained by the tensile tests at 890 °C and $1\times 10^{-3} \text{ s}^{-1}$ also validate the effectiveness of the constitutive model, as shown in Fig. 10(a) in the dotted line. It shows that a good agreement for experimental data and calculated results has been obtained. Thus, the constitutive model established in this work can describe the microstructure evolution for Ti–6Al–4V alloy during the superplastic forming.

Figure 11 describes the ratio of HAGBs area to GBs area for the deformation of Ti–6Al–4V alloy at 920 °C. For $\dot{\varepsilon}=1\times 10^{-2} \text{ s}^{-1}$, the ratio of HAGBs area to the GBs area increases with the deformation process. It is indicated that there is larger a HAGBs area, which is due to lots of sub-grain boundaries evolving into grain boundaries caused by CDRX. After recrystallization, the number of fine grains increases, and the area of HAGBs increases.

The evolution of the normalized misorientation angle $\bar{\theta}_{sub}$ is given in Fig. 12. The normalized misorientation increases with the increase of strain

Table 2 Parameters optimized for grain size constitutive model

β_1	β_2	β_3	β_4	β_5	C_{a_1}	C_{a_2}	C_{a_3}	C_{a_4}
27.57	24.42	5.31	1.59	0.072	0.11	2530793	293994.5	2.24
C_{a_5}	C_{a_6}	θ_r	γ_1	γ_2	γ_3	γ_4	γ_5	γ_6
40535.45	4154124	0.95	1.27	0.38	1.46	0.46	0.02	0.51
γ_7	γ_8	γ_9	γ_{10}	γ_{11}	n	γ_θ	$Q_a/(\text{J}\cdot\text{mol}^{-1})$	$Q_b/(\text{J}\cdot\text{mol}^{-1})$
3.28	0.04	0.40	3.51	0.25	1.05	1.48	46980.8	21737.98

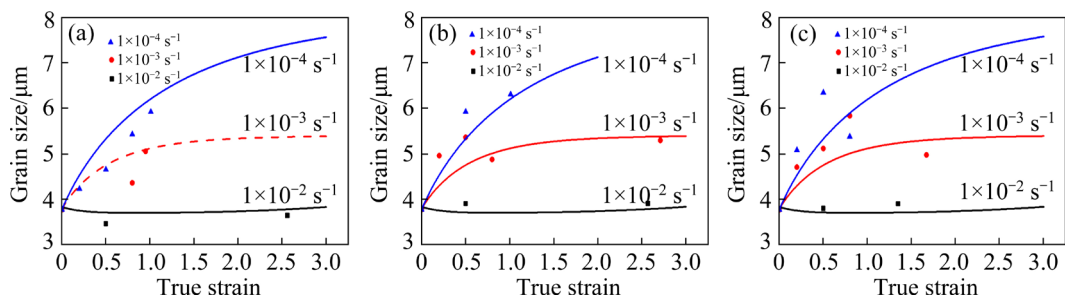


Fig. 10 Comparison between experimental data and predicted results: (a) 890 °C; (b) 920 °C; (c) 950 °C

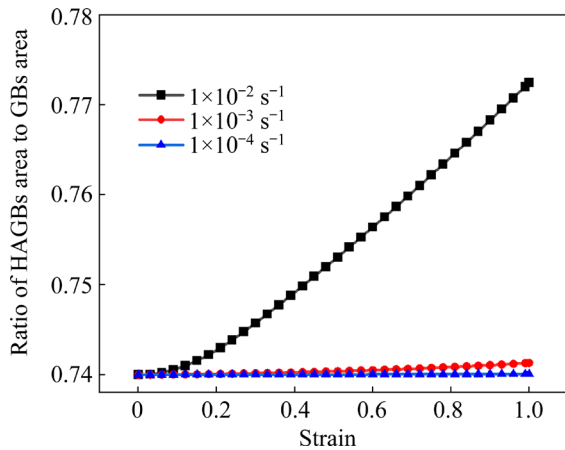


Fig. 11 Ratio of HAGBs area to GBs area for Ti-6Al-4V alloy at 920 °C

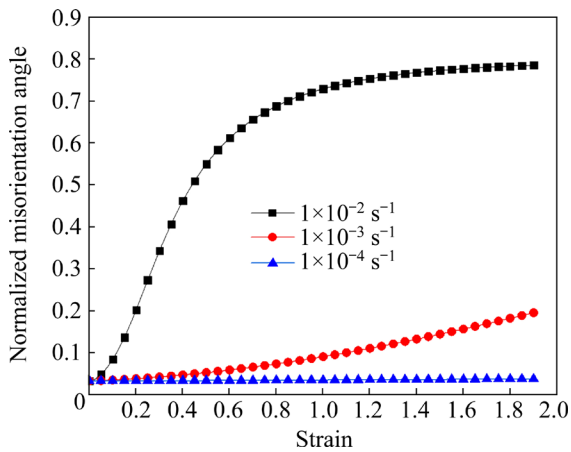


Fig. 12 Evolution of normalized misorientation angle $\bar{\theta}_{\text{sub}}$ by constitutive model at 920 °C

rate. For the CDRX at the strain rate of $1 \times 10^{-2} \text{ s}^{-1}$, the misorientation of LAGBs gradually increases, and the reason for this is that this process requires deformation accumulation. The grain rotation has been discussed in other papers, but the sub-grain rotation is always ignored, which is well verified by the calculation results of normalized misorientation angle. The normalized misorientation angle will reach a stable value after increasing to 0.78, in other words, the maximum LAGBs misorientation angle is about 11.7° . This phenomenon can be explained as follows: In the CDRX process, the sub-grain will rotate when the misorientation angle of LAGBs increases to a value less than 15° . The θ_{sub} of Sub-grain B5 is 9.01° in Fig. 9, which does not reach the $\theta_{\text{sub}}=15^\circ$ for the critical value of new recrystallized grains. However, Sub-grain B5 has been verified in a different orientation from the parent grain in Fig. 8. When the misorientation of

LAGBs increases to a saturated value, the dislocation motion is not capable of driving the evolution of LAGBs, so the gap between the saturated misorientation and critical value (15°) must rely on the sub-grain rotation. Therefore, in the process of grain refinement, the misorientation of LAGBs increases to a saturated value, which is numerically less than 15° . The evolution of misorientation during the CDRX process can be divided into two stages: (1) evolution by dislocation movement before the saturated misorientation; (2) evolution by sub-grain rotation between the saturated and critical misorientations.

4.4 Evolution mechanism of grain boundary misorientation during CDRX

The evolution mechanism of CDRX is illustrated in Fig. 13. During the superplastic deformation of Ti-6Al-4V alloy, the CDRX process is essentially the conversion of the area between HAGBs and LAGBs. The evolution of the grain boundary misorientation is caused by the redistribution of GNDs density, which is affected by the dislocation movement. Firstly, there is a phenomenon of mutual migration between the LAGBs and the HAGBs, and the HAGBs will also sweep the LAGBs of the path during the migration process. Secondly, dislocations near LAGBs tend to accumulate towards LAGBs and increase the misorientation. Thirdly, the rotation will occur between sub-grains, which will also promote the evolution from LAGBs to HAGBs. Besides, the sub-grain rotation will be observed before the completion of the CDRX process. Particularly, the first two mechanisms are dominant until the grain boundary misorientation reaches a saturated value; otherwise, the sub-grain rotation will be activated.

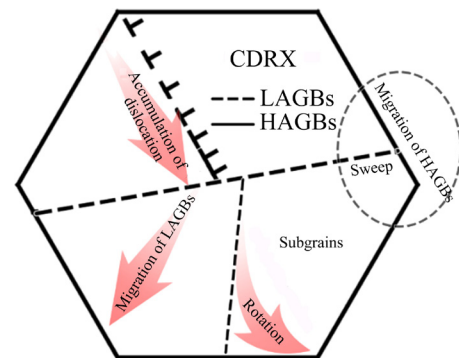


Fig. 13 Mechanism of evolution for LAGBs and HAGBs during CDRX

5 Conclusions

(1) The mechanism of the CDRX has been discussed, especially in the sub-grain rotation.

(2) During the superplastic deformation at 890–950 °C, the CDRX is the dominant mechanism with the redistribution of GNDs densities.

(3) The migrations of the LAGBs and HAGBs occur simultaneously, meaning that the fine grains are recrystallized when the LAGBs transform to the HAGBs.

(4) The sub-grain rotation starts playing a significant role after the LAGBs misorientation reaches the saturated values, which has been verified by observed results before the critical misorientation.

Acknowledgments

The authors are grateful for the financial support from the Key Research and Development Program of Shaanxi Province, China (No. 2020ZDLGY01-05).

References

- [1] YASMEEN T, ZHAO Bing, ZHENG Jing-hua, TIAN Fa-min, LIN Jian-guo, JIANG Jun. The study of flow behavior and governing mechanisms of a titanium alloy during superplastic forming [J]. *Materials Science and Engineering A*, 2020, 788: 139482.
- [2] ZHU Yun-long, ZHAO Qing-long, JIANG Qi-chuan, LIU Xiao, GENG Run, WANG Bao. Improved strength-ductility of Ti–6Al–4V casting alloys with trace addition of TiC–TiB₂ nanoparticles [J]. *Nanomaterials*, 2020, 10(12): 2330.
- [3] BANERJEE D, WILLIAMS J C. Perspectives on titanium science and technology [J]. *Acta Materialia*, 2013, 61(3): 844–879.
- [4] KOPEC M, WANG Ke-huan, POLITIS D J, WANG Yao-qi, WANG Li-liang, LIN Jian-guo. Formability and microstructure evolution mechanisms of Ti6Al4V alloy during a novel hot stamping process [J]. *Materials Science and Engineering A*, 2018, 719: 72–81.
- [5] LIU Jian, KHAN A S, TAKACS L, MEREDITH C S. Mechanical behavior of ultrafine-grained/nanocrystalline titanium synthesized by mechanical milling plus consolidation: Experiments, modeling and simulation [J]. *International Journal of Plasticity*, 2015, 64: 151–163.
- [6] LIN Peng, XI Xian-zheng, ZHAO Wen-kai, YANG Rui-hong, LIN Fei, CUI Xiao-lei, LIU Gang. Microstructure and mechanical properties of Ti–6Al–4V/Ti–22Al–25Nb joint formed by diffusion bonding [J]. *Transactions of Nonferrous Metals Society of China*, 2021, 31(5): 1339–1349.
- [7] RATOCHKA I, LYKOVA O, MISHIN I, NAYDENKIN E. Superplastic deformation behavior of Ti–4Al–2V alloy governed by its structure and precipitation phase evolution [J]. *Materials Science and Engineering A*, 2018, 731: 577–582.
- [8] WANG Gang, ZHANG Wen-cong, ZHANG Gong-lei, XU Zhi-liang. Superplastic formability of Ti–6Al–4V butt-welded plate by laser beam welding [J]. *Transactions of Nonferrous Metals Society of China*, 2009, 19(2): 429–433.
- [9] WU Yong, WU Di-peng, MA Jia, XIAO Wen-chao, ZHENG Kai-lun, CHEN Min-he. A physically based constitutive model of Ti–6Al–4 V and application in the SPF/DB process for a pyramid lattice sandwich panel [J]. *Archives of Civil and Mechanical Engineering*, 2021, 21: 1–17.
- [10] ALABORT E, KONTIS P, BARBA D, DRAGNEVSKI K, REED R C. On the mechanisms of superplasticity in Ti–6Al–4V [J]. *Acta Materialia*, 2016, 105: 449–463.
- [11] YAKOVITSEVA O A, MIKHAYLOVSKAYA A V, MOCHUGOVSKIY A G, CHEVERIKIN V V, PORTNOY V K. Superplastic deformation mechanisms in high magnesium contenting aluminum alloy [J]. *Materials Science Forum*, 2016, 838/839: 66–71.
- [12] DUAN Yu-lu, XU Guo-fu, ZHOU Li-qi, XIAO Dan, DENG Ying, YIN Zhi-min, PENG Bing, PAN Qing-lin, WANG Ying-jun, LU Li-ying. Achieving high superplasticity of a traditional thermal-mechanical processed non-superplastic Al–Zn–Mg alloy sheet by low Sc additions [J]. *Journal of Alloys and Compounds*, 2015, 638: 364–373.
- [13] KOTOV A D, MIKHAYLOVSKAYA A V, KISHCHIK M S, TSARKOV A A, AKSENOV S A, PORTNOY V K. Superplasticity of high-strength Al-based alloys produced by thermomechanical treatment [J]. *Journal of Alloys and Compounds*, 2016, 688: 336–344.
- [14] MIKHAYLOVSKAYA A V, YAKOVITSEVA O A, GOLOVIN I S, POZDNIAKOV A V, PORTNOY V K. Superplastic deformation mechanisms in fine-grained Al–Mg based alloys [J]. *Materials Science and Engineering A*, 2015, 627: 31–41.
- [15] MIKHAYLOVSKAYA A V, YAKOVITSEVA O A, SITKINA M N, KOTOV A D, IRZHAK A V, KRYMSKIY S V, PORTNOY V K. Comparison between superplastic deformation mechanisms at primary and steady stages of the fine grain AA7475 aluminium alloy [J]. *Materials Science and Engineering A*, 2018, 718: 277–286.
- [16] RUST M A, TODD R I. Surface studies of region II superplasticity of AA5083 in shear: Confirmation of diffusion creep, grain neighbour switching and absence of dislocation activity [J]. *Acta Materialia*, 2011, 59: 5159–5170.
- [17] MASUDA H, SATO E. Diffusional and dislocation accommodation mechanisms in superplastic materials [J]. *Acta Materialia*, 2020, 197: 235–252.
- [18] YANG Jun-zhou, WU Jian-jun. Grain rotation accommodated GBS mechanism for the Ti–6Al–4V alloy during superplastic deformation [J]. *Crystals*, 2021, 11(8): 991.
- [19] TAYLOR S, WEST G D, MOGIRE E, TANG F, KOTADIA H R. Superplastic forming characteristics of AZ41 magnesium alloy [J]. *Transactions of Nonferrous Metals Society of China*, 2021, 31(3): 648–654.

- [20] SITDIKOV O, AVTOKRATOVA E, LATYPOVA O, MARKUSHEV M. Structure, strength and superplasticity of ultrafine-grained 1570C aluminum alloy subjected to different thermomechanical processing routes based on severe plastic deformation [J]. Transactions of Nonferrous Metals Society of China, 2021, 31(4): 887–900.
- [21] YANG Jun-zhou, WU Jian-jun, ZHANG Qian-wen, HAN Ruo-lan, WANG Kai-wei. Investigation of flow behavior and microstructure of Ti–6Al–4V with annealing treatment during superplastic forming [J]. Materials Science and Engineering A, 2020, 797: 140046.
- [22] ALABORT E, BARBA D, SHAGIEV M R, MURZINOVA M A, GALEYEV R M, VALIAKHMETOV O R. Alloys-by-design: Application to titanium alloys for optimal superplasticity [J]. Acta Materialia, 2019, 178: 275–287.
- [23] FAKHAR N, SABBAGHIAN M, NAGY P, FEKETE K, GUBICZA J. Superior low-temperature superplasticity in fine-grained ZK60 Mg alloy sheet produced by a combination of repeated upsetting process and sheet extrusion [J]. Materials Science and Engineering A, 2021, 819: 141444.
- [24] YANG Wen-peng, GUO Xue-peng, YANG Kai-jun. Low temperature quasi-superplasticity of ZK60 alloy prepared by reciprocating extrusion [J]. Transactions of Nonferrous Metals Society of China, 2012, 22(2): 255–261.
- [25] SHI Xiao-hui, CAO Zu-han, FAN Zhi-yuan, ECKERT J, QIAO Jun-wei. Static coarsening behavior of equiaxed α phase in Ti–8Al–1Mo–1V alloy [J]. Transactions of Nonferrous Metals Society of China, 2021, 31(6): 1628–1640.
- [26] CHUVIL'DEEV V N, GRYAZNOV M Y, SHOTIN S V, KOPYLOV VI, NOKHRIN A V, LIKHNITSKII C V, MURASHOV A A, BOBROV A A, TABACHKOVA N Y, PIROZHNIKOVA O E. Investigation of superplasticity and dynamic grain growth in ultrafine-grained Al–0.5%Mg–Sc alloys [J]. Journal of Alloys and Compounds, 2021, 877: 160099.
- [27] ALABORT E, PUTMAN D, REED R C. Superplasticity in Ti–6Al–4V: Characterisation, modelling and applications [J]. Acta Materialia, 2015, 95: 428–442.
- [28] LIU Jin-xue, LIU Ke, DU Wen-bo, LI Shu-bo, WANG Zhao-hui, DU Xiao, SUN Cui-cui. Effect of temperature on microstructure and texture evolution of Mg–Zn–Er alloy during hot compression [J]. Transactions of Nonferrous Metals Society of China, 2018, 28(11): 2214–2225.
- [29] QIANG Feng-ming, BOUZY E, KOU Hong-chao, ZHANG Yu-dong, WANG Ling-ling, LI Jin-shan. Grain fragmentation associated continuous dynamic recrystallization (CDRX) of hexagonal structure during uniaxial isothermal compression: High-temperature α phase in TiAl alloys [J]. Intermetallics, 2021, 129: 107028.
- [30] YAMANE G, AVOTRINIAINA F, IMAI H, SONG L, VIDAL V, MATSUMOTO H, VELAY V. Experimental study of the superplastic and hot deformation mechanisms of a Ti–6Al–2Sn–4Zr–2Mo titanium alloy [C]//Proceedings of the 14th World Conference on Titanium. Nantes, France, 2020.
- [31] MATSUMOTO H, NAITO D, MIYOSHI K, YAMANAKA K, CHIBA A, YAMABE-MITARAI Y. Forging property, processing map, and mesoscale microstructural evolution modeling of a Ti-17 alloy with a lamellar ($\alpha+\beta$) starting microstructure [J]. Science and Technology of Advanced Materials, 2017, 18(1): 893–904.
- [32] MATSUMOTO H, YAMANAKA K, CHIBA A, YAMABE-MITARAI Y, ITSUMI Y. Macro-mesoscale microstructural evolution modeling under hot forging of a Ti-17 alloy with a lamellar ($\alpha+\beta$) starting microstructure [C]//Proceedings of the 14th World Conference on Titanium. Nantes, France, 2020.
- [33] LUO Jiao, LI Miao-quan, LI Xiao-li, SHI Yan-pei. Constitutive model for high temperature deformation of titanium alloys using internal state variables [J]. Mechanics of Materials, 2010, 42(2): 157–165.
- [34] YANG Jun-zhou, WU Jian-jun, YANG Dong-shen, WANG Qi-shuai, WANG Kai-wei, ZHANG Zeng-kun. A modified constitutive model with grain rotation for superplastic forming of Ti–6Al–4V alloy [J]. Journal of Engineering Materials and Technology, 2020, 142: 1–13.
- [35] GOURDET S, MONTHEILLET F. A model of continuous dynamic recrystallization [J]. Acta Materialia, 2003, 51(9): 2685–2699.
- [36] SUN Z C, WU H L, CAO J, YIN Z K. Modeling of continuous dynamic recrystallization of Al–Zn–Cu–Mg alloy during hot deformation based on the internal-state-variable (ISV) method [J]. International Journal of Plasticity, 2018, 106: 73–87.
- [37] LI Yi-bo, GU Bin, JIANG Shuai, LIU Yao-qiong, SHI Zhu-sheng, LIN Jian-guo. A CDRX-based material model for hot deformation of aluminium alloys [J]. International Journal of Plasticity, 2020, 134: 102844.
- [38] WU Yong, FAN Rong-lei, CHEN Ming-he, WANG Ke-huan, ZHAO Jie, XIAO Wen-chao. High-temperature anisotropic behaviors and microstructure evolution mechanisms of a near- α Ti-alloy sheet [J]. Materials Science and Engineering A, 2021, 820: 141560.
- [39] BAO Jian-xing, LV Shou-dan, ZHANG Mei-wei, SHAN De-bin, GUO Bin, XU Jie. Multi-scale coupling effects on flow localization during micro-compression deformation of Ti–6Al–4V alloy [J]. Materials Science and Engineering A, 2020, 793: 139888.
- [40] LI Dong-peng, ZHANG Duan-zheng, LIU Sheng-dan, SHAN Zhao-jun, ZHANG Xin-ming, WANG Qin, WANG Qin, HAN Su-qi. Dynamic recrystallization behavior of 7085 aluminum alloy during hot deformation [J]. Transactions of Nonferrous Metals Society of China, 2016, 26(6): 1491–1497.
- [41] DRIVER J. The limitations of continuous dynamic recrystallization (CDRX) of aluminium alloys [J]. Materials Letters, 2018, 222: 135–137.
- [42] PATNAMSETTY M, SOMANI M C, GHOSH S, AHMED S, PEURA P. Processing map for controlling microstructure and unraveling various deformation mechanisms during hot working of CoCrFeMnNi high entropy alloy [J]. Materials Science and Engineering A, 2020, 793: 139840.
- [43] ZHAO Shi-lin, ZHANG Hai-ming, CUI Zhen-shan, CHEN Dong, CHEN Zhe. Superplastic behavior of an in-situ TiB₂ particle reinforced aluminum matrix composite processed by elliptical cross-section torsion extrusion [J]. Materials

- Characterization, 2021, 178: 111243.
- [44] PANTLEON W. Resolving the geometrically necessary dislocation content by conventional electron backscattering diffraction [J]. Scripta Materialia, 2008, 58(11): 994–997.
- [45] HUANG Lin-jie, QI Feng, YU Lian-xu, XIN Xin, LIU Fang, SUN Wen-ru, HU Zhuang-qi. Necking behavior and microstructural evolution during high strain rate superplastic deformation of IN718 superalloy [J]. Materials Science and Engineering A, 2015, 634: 71–76.
- [46] BEUCIA B, QUEYREAU S, KAHLOUN C, CHAUBET D, FRANCIOSI P, BACROIX B. Plastic strain-induced grain boundary migration (SIBM) in pure aluminum: SEM in-situ and AFM examinations [J]. International Journal of Plasticity, 2019, 115: 29–55.
- [47] LIN J, LIU Y, FARRUGIA D C J, ZHOU M. Development of dislocation-based unified material model for simulating microstructure evolution in multipass hot rolling [J]. Philosophical Magazine, 2005, 85: 1967–1987.
- [48] LU Y, ARISTIZABAL M, WANG X, PANG B, CHIU Y L, KLOENNE Z T, FRASER H L, LORETTO M H. The influence of heat treatment on the microstructure and properties of HIPped Ti–6Al–4V [J]. Acta Materialia, 2019, 165: 520–527.
- [49] DUAN X, SHEPPARD T. Simulation of substructural strengthening in hot flat rolling [J]. Journal of Materials Processing Technology, 2002, 125/126: 179–187.
- [50] LIN Jian-guo, YANG Jian-bo. GA-based multiple objective optimization for determining viscoplastic constitutive equations for superplastic alloys [J]. International Journal of Plasticity, 1999, 15(11): 1181–1196.

Ti–6Al–4V 钛合金超塑成形 连续动态再结晶机理及亚晶粒转动

杨俊宙, 吴建军, 谢海南, 李志国, 王凯伟

西北工业大学 机电学院, 西安 710072

摘要: 研究 Ti–6Al–4V 合金在超塑性成形过程中的连续动态再结晶机理, 并重点研究取向差演变机制。在温度为 890、920 和 950 °C, 应变速率为 10^{-4} ~ 10^{-2} s⁻¹ 的条件下进行拉伸试验, 采用电子背散射衍射与本构模型相结合的方法描述显微组织演变。几何必需位错在小角晶界处形成过程中起作用。此外, 小角晶界转化为大角晶界的机制包括: (1)大角晶界向小角晶界的迁移; (2)由动态回复不充分的残余位错在小角晶界处聚集; (3)亚晶粒的旋转也会促进晶粒形核。基于物理本构模型的计算结果, 验证在小角晶界转变为大角晶界前亚晶粒会发生旋转。特别地, 在晶界角取向差的演化过程中, 位错运动在取向差达到饱和值前起主导作用, 否则亚晶粒旋转将起主导作用。

关键词: 连续动态再结晶; 亚晶粒旋转; 晶界角取向差; 超塑变形

(Edited by Wei-ping CHEN)